Supporting Information for "Quantifying Regional Efficiency of Marine Carbon Dioxide Removal (mCDR) via Alkalinity Enhancement using the ECCO-Darwin Ocean Biogeochemistry State Estimate and an Idealized Vertical 1-D Model"

Kay Suselj[1], Dustin Carroll[2,1], Dimitris Menemenlis[1], Hong Zhang[1], Nate Beatty[3], Anna Savage[3], Daniel Whitt[4],

[1]Jet Propulsion Laboratory, California Institute of Technology, Pasadena, CA, USA

[2]Moss Landing Marine Laboratories, San José State University, Moss Landing, CA, USA

[3]Running Tide, Inc., Portland, ME, USA

[4]NASA Ames Research Center, Moffett Field, CA, USA

Contents of this file

Text S1. Validation of Baseline ECCO-Darwin Simulation.

Figure S1 compares the key time-mean surface-ocean fields that impact CO_2 solubility from baseline ECCO-Darwin vs. reference datasets. This comparison highlights the essential ocean conditions characterized by both chemical and physical/dynamical processes and provides the evidence that ECCO-Darwin credibly represents the processes crucial for simulating OAE. Reference sea-surface temperature (SST) is derived from optimally-interpolated satellite and in-situ observations using the methodology of Reynolds, Rayner, Smith, Stokes, and Wang (2002). Sea-surface salinity (SSS), dissolved inorganic carbon (DIC), and Alk are from the OceanSODA-ETHZ dataset (Gregor & Gruber, 2021), which leverages a suite of observations and a two-step approach (cluster-regression) to construct gridded monthly-mean fields that represent the global-ocean carbonate system.

The key aspects of ECCO-Darwin shown on Figure S1 are as follows:

• Polarward decrease of SST as well as the zonal gradient observed across ocean basins (Figure S1a). The latter feature is attributed to meridional transport by large-scale ocean gyres.

• Polarward decrease of SSS and Alk and maximum values located in subtropical regions associated with high rates of evaporation (Figure S1b,d). The lowest values are located in regions that exhibit significant sea-ice melt and/or intense precipitation.

• Poleward increase of DIC with significant hemispheric asymmetry. The lowest DIC values are generally found in the tropics, which are associated with increased biological productivity resulting from by upwelling-driven nutrient supply (Figure S1c).

Figure S1 shows additional validation for the 5 OAE locations: a scatter-plots of DIC and Alk profile from baseline ECCO-Darwin simulations against in-situ GLODAPv2.2022

observations (Olsen et al., 2020) at the 5 deployment sites studied in this work. For all five locations, both DIC and Alk from ECCO-Darwin generally reproduce observations, which demonstrates that ECCO-Darwin captures the key biogeochemical variables relevant for OAE studies in these regions. Figure S3 compares key surface-ocean variables from the previously-published ECCO-Darwin LLC 270 solution (Carroll et al., 2020) against the LLC90 ECCO-Darwin version used in this work. The agreement between the two solutions shows that there is no need for further parameter tuning in the LLC90 set-up.

Text S2. Quantification of OAE Additionality.

In this section, we describe representation of OAE additionality as a function of different process-based components and in Supporting Information Text S3 and S4 we describe how these components are estimated from ECCO-Darwin simulations. We first consider a pulse OAE deployments (in which a short Alk pulse is deployed to the surface ocean) and then generalize the description to deployments with known time-dependent Alk flux.

1) Pulse OAE deployment

Pulse OAE deployments are such that Alk is injected in the surface ocean over a small area (a_0) at time (t) instantaneously (i.e., over much shorter timescales than the multi-annual timescale associated with atmospheric CO_2 uptake). The OAE additionality (i.e. horizontally-integrated net CO_2 flux from the atmosphere attributed to OAE) Δf_{CO_2} (in mol C per second) at time τ ($\tau > t$) can be written similar to e.g. Wang et al. (2023) as:

$$\Delta f_{CO_2}(\tau) = \Delta Alk \times mCDR_{pot}(t, a_0) \times mCDR_{exch}(\tau - t, t, a_0), \quad (1)$$

where $\tau - t$ represents time after Alk injection.

To arrive to Equation 1, the following processes are assumed. After Alk is injected, aqueous CO_2 disassociates into bicarbonate and carbonate ions through a series of rapid acid-base reactions; this chemical adjustment leads to a reduction in partial pressure of CO_2 in seawater (pCO_2). The mCDR potential, $mCDR_{pot}$ represents the amount of carbon the seawater needs to uptake from the atmosphere in order for pCO_2 to reequilibrate back to its state prior to OAE deployment (per unit of injected Alk) and is generally a function of location and time of Alk injection and can be approximated as:

$$mCDR_{pot}(t, a_0) \equiv \frac{\partial DIC}{\partial Alk}\Big|_{pCO_2}(t, a_0). \tag{2}$$

where the partial derivative in Equation 2 is estimated for constant pCO_2, indicated by the subscript.

The $mCDR_{exch}$ (in units of inverse seconds) represents the normalized uptake rate of CO_2 from the atmosphere and is a function of elapsed time after Alk injection, $\tau - t$, as well as time and the location of Alk injection.

Equation 1 conveniently separates the impact of OAE into: 1) its potential, $mCDR_{pot}$ a function of CO_2 solubility and 2) dynamical processes in the ocean, ocean-atmosphere interactions, interactions between ocean dynamics and solubility, and feedbacks that influence the rate of CO_2 uptake represented by $mCDR_{exch}$. In the absence of other feedbacks except for reequilibration of ocean carbonate species, $mCDR_{exch}$ is dominated by ocean dynamics and the rate of air-sea CO_2 exchange.

The key assumptions in deriving Equation 1 are:

- The value of $mCDR_{pot}$ is taken at the deployment location and time; however, its values over the surface area of OAE-attributed CO_2 uptake is relevant (i.e., as the per-

turbation spreads we expect these two surface areas to differ). Because the $mCDR_{pot}$ varies slowly with time and across ocean basins, the difference between the two values of $mCDR_{pot}$ are small and the difference between the two $mCDR_{pot}$ values is implicitly included in $mCDR_{exch}$.

- We assume that the amount of injected Alk is small, so that CO_2 solubility does not change substantially and thus $mCDR_{pot}$ is not modified.

Integrating Equation 1 in time from t to τ to yields an expression for the total cumulative OAE additionality:

$$\Delta F_{CO_2}(\tau) = \Delta Alk \times mCDR_{pot}(t, a_0) \times mCDR_{eff}(\tau - t, t, a_0), \tag{3}$$

where dynamical mCDR efficiency is defined as:

$$mCDR_{eff}(\tau - t, t, a_0) \equiv \int_t^\tau mCDR_{exch}(\tau - t', t, a_0)\, \mathrm{d}t'. \tag{4}$$

where t' in integration variable. $mCDR_{eff}$ is termed dynamical efficiency because its value represents a fraction of $mCDR_{pot}$ that has been realized by time $\tau - t$ after OAE injection; this is in the absence of other feedbacks and $mCDR_{eff}$ ranges between 0–1. While $mCDR_{exch}$ and $mCDR_{eff}$ are equivalent, we often use the latter as its interpretation is more straightforward. Therefore, if we characterize the values of $mCDR_{pot}$ and $mCDR_{eff}$ over the global ocean, Equation 3 quantifies the amount of OAE-attributed atmospheric CO_2 uptake for any pulse OAE deployment.

(b) Generalizing pulse OAE Deployments

It is unlikely that real-world OAE deployments can be considered pulse deployments. Quantification of OAE additionality for deployment at location a_0 can be quantified by

generalizing Equation 3. If the OAE deployment starts at time t_s, with a specified rate of Alk injection $f_{Alk}(t)$ (in units of mol Alk per second), the OAE additionality at time τ ($\tau > t_s$) can be approximated as:

$$\Delta f_{CO_2}(\tau) = \int_{t_s}^{\tau} f_{Alk}(t) \times mCDR_{pot}(t) \times mCDR_{exch}(\tau - t, t, a_0)\, \mathrm{d}t, \tag{5}$$

where Equation 5 is derived by integrating Equation 1 over time (representing deployment increments). As before, we assume that Alk injected by OAE is small and its impact on carbon uptake is linear, i.e., OAE does not substantially modify the values of $mCDR_{pot}$ and $mCDR_{exch}$.

The cumulative OAE additionality at time τ is then:

$$\Delta F_{CO_2}(\tau) = \int_{t_s}^{\tau} f_{Alk}(t) \times mCDR_{pot}(t, a_0) \times mCDR_{eff}(\tau - t, t, a_0)\, \mathrm{d}t. \tag{6}$$

In the next section, we discuss the design of ECCO-Darwin numerical experiments and the use of auxiliary data to evaluate both $mCDR_{pot}$ and $mCDR_{eff}$.

Text S3. Estimation of mCDR potential.

We estimate $mCDR_{pot}$ following Equation 2 considering the full carbon chemistry, as:

$$mCDR_{pot} = \frac{DIC(pCO_2, Alk + \delta Alk, SST, SSS) - DIC(pCO_2, Alk, SST, SSS)}{\delta Alk}, \tag{7}$$

where DIC as a function of $p\mathrm{CO}_2$ Alk, sea-surface-temperature (SST), and sea-surface salinity (SSS) is estimated using the PyCO2SYS (Humphreys et al., 2022) carbonate system. In this computation, the concentration of borate and minor ions are taken to be a function of salt concentration, as it is usually done. We take $\delta Alk = 100$ μmol kg^{-1}.

The results are not sensitive to the exact value of δAlk and we use the monthly-mean values of surface ocean state.

In this approach, $mCDR_{pot}$ can thus be estimated from the baseline state of the ocean (without considering the specific OAE approach) from ECCO-Darwin or any other dataset that include required inputs for Equation 7. Here, $mCDR_{pot}$ is estimated from both the baseline ECCO-Darwin and OceanSODA-ETHZ (Gregor & Gruber, 2021) datasets.

Text S4. ECCO-Darwin Simulations for Estimation of Dynamic mCDR Efficiency

1) Pulse OAE Experiment

Unlike mCDR potential, which can be estimated from the ocean state, this is not the case for dynamic mCDR efficiency, $mCDR_{eff}$. The most straightforward way of estimating it is performing pulse OAE experiments with an ocean biogeochemistry model (such as ECCO-Darwin) in which Alk is injected at time t and a_0. The $mCDR_{eff}$ can be estimated following Equation 3 as:

$$mCDR_{eff}(\tau - t, t, a_0) = \frac{\Delta F_{CO_2}(\tau)}{\Delta Alk \times mCDR_{pot}(t, a_0)}, \tag{8}$$

where ΔF_{CO_2} is the model-estimated cumulative OAE additionality at time τ, ΔAlk is the amount of injected Alk, and as before the mCDR potential $mCDR_{pot}$ is taken at the time and location of OAE deployment.

2) Continuous OAE Experiment

Alternatively, we propose to use continuous numerical OAE experiments for better quantification of overall mCDR efficiency. For these experiments, a constant Alk flux,

f_{Alk}, over surface area a_0 is continuously injected into the surface ocean starting at time t_s. We first define mCDR efficiency for a continuous experiment, $mCDR_{eff}^{cont}$, as:

$$mCDR_{eff}^{cont}(\tau - t_s, t_s, a_0) \equiv \int_{t_s}^{\tau} mCDR_{exch}(\tau - t', t', a_0)\,\mathrm{d}t'. \tag{9}$$

Following Equation 5, the mCDR efficiency can be estimated with continuous OAE experiments as:

$$mCDR_{eff}^{cont}(\tau - t_s, t_s, a_0) = \frac{f_{Alk} \times \overline{mCDR_{pot}(t, a_0)\Big|_{t_s}^{\tau}}}{\Delta f_{CO_2}(\tau)}, \tag{10}$$

where $mCDR_{pot}$ is the time mean over the interval $[t_s\ \tau]$, which is indicated by the overline.

How are $mCDR_{eff}^{cont}$ and $mCDR_{eff}$ related? From their definitions (Equations 4 and 10), it is apparent that they are exactly equal if the $mCDR_{exch}$ (or $mCDR_{eff}$) is independent on deployment time. If that is not the case, $mCDR_{eff}^{cont}$ represents the time-mean value of $mCDR_{eff}$ over the injection times of continuous experiment. We therefore propose that the $mCDR_{eff}^{cont}$ better characterizes the overall efficiency of deployments and thus use continuous OAE experiments for characterization of deployment sites.

For the sites in which we find significant seasonal variability in $mCDR_{eff}^{cont}$, we designed additional pulse experiments to identify the relationship between seasonal OAE deployment and seasonal variability of $mCDR_{eff}^{cont}$.

3) Solubility Effect on Efficiency

In the discussion above, we considered the $mCDR_{pot}$ at the location and time of Alk injection (i.e. see Equation 1), while its values at the location and time of OAE-attributed CO_2 uptake are relevant values that describe mCDR potential. In our definition of ef-

ficiencies, the difference between the values of $mCDR_{pot}$ over the two regions effectively modifies $mCDR_{eff}$ for pulse or $mCDR_{eff}^{cont}$ for continuous OAE experiments.

The ratio between the $mCDR_{pot}$ at the OAE-attributed CO_2 uptake and its values over the deployment location therefore represent multiplicative factor with which mCDR efficiencies should be modified to account for this solubility effect, and is the ratio between the $mCDR_{pot}$ for the two locations:

$$mCDR_{sol}^{eff}(\tau, a_0) = \frac{\overline{mCDR_{pot}(\tau, a_{exch})}}{mCDR_{pot}(t, a_0)}, \tag{11}$$

where $\overline{mCDR_{pot}(\tau, a_{exch})}$ represents the horizontal area-weighted mean of $mCDR_{pot}$ where OAE attributed air-sea CO_2 exchange occurs. In our analysis, we take the OAE-attributed CO_2 exchange to be proportional to the magnitude of the OAE-modified partial pressure of CO_2 in the surface ocean (Δp_{CO_2}).

4) mCDR Equilibration Coefficient

To quantify CO_2 reequilibration of OAE-impacted seawater, and to track the transport of seawater in disequilibrium, we define the mCDR equilibration coefficient $mCDR_{equil}$ similar to Wang et al. (2023), as a fraction of the realized potential of CO_2 uptake:

$$mCDR_{equil} = \frac{1}{\overline{mCDR_{pot}}} \frac{\Delta DIC}{\Delta Alk} \tag{12}$$

where $mCDR_{pot}$ is the time-mean value over the duration of Alk perturbation at the deployment site. $mCDR_{equil}$ represents the fraction of potential CO_2 uptake that has been realized in a volume of seawater for a given Alk increase and is thus similar to mCDR efficiency, where a value of one indicates that the full potential has been realized. Unlike $mCDR_{eff}$ (or $mCDR_{eff}^{cont}$), which quantifies a fraction of potential CO_2 uptake for

the entire deployment, $mCDR_{equil}$ is a local value computed for a particular volume of seawater.

Text S5. Budgets of DIC and Alk Perturbations due to OAE

To quantify vertical mixing and dynamics of Alk and DIC perturbations and their interaction with additional OAE additionality, we derive horizontal-mean equations for Alk and DIC perturbations, as described below. We begin with the budget equations for these two quantities as represented in ECCO-Darwin (Carroll et al., 2022):

$$\frac{\partial DIC}{\partial t} = -\nabla(\vec{u} \cdot DIC) + \nabla K(\nabla DIC) + \frac{\partial DIC}{\partial t}\Big|_{bio} + \frac{\partial DIC}{\partial t}\Big|_{dillution} + \frac{\partial f_{atm}^{CO_2}}{\partial z} \text{ and } \quad (13)$$

$$\frac{\partial Alk}{\partial t} = -\nabla(\vec{u} \cdot Alk) + \nabla K(\nabla Alk) + \frac{\partial Alk}{\partial t}\Big|_{bio} + \frac{\partial Alk}{\partial t}\Big|_{dillution} + \frac{\partial f_{Alk}}{\partial z}, \quad (14)$$

where symbols $\vec{u}$ and K are the 3-D velocity and diffusivity fields.

The terms on the left-hand-side of Equations 13 and 14 represent tendency terms. The first two terms on the right-hand-side of the two equations are resolved advection and parameterized turbulent and molecular diffusion, the third term (with the subscript *bio*) represents biological impacts, and the forth term (with the subscript *dillution*) represents dilution due to freshwater flux through precipitation and river runoff, and the last terms represent the air-sea CO_2 exchange and Alk flux for DIC and Alk, respectively.

Next, we horizontally integrate Equations 13 and 14 over the global ocean and compute the difference of the budget terms for the OAE-perturbed and baseline simulation to obtain the following two equations for DIC and Alk perturbations:

$$\underbrace{\frac{\partial}{\partial t}\widehat{\Delta DIC}}_{\text{tendency}} = \underbrace{-\frac{\partial}{\partial z}\widehat{w\Delta DIC}}_{\text{advection}} + \underbrace{\frac{\partial}{\partial z}\widehat{K\frac{\partial}{\partial z}\Delta DIC}}_{\text{diffusion}} + \underbrace{\frac{\partial}{\partial t}\widehat{\Delta DIC|_{bio}}}_{\text{biology}} + \underbrace{\frac{\partial}{\partial z}\widehat{\Delta f_{atm}^{CO_2}}}_{CO_2\text{ flux}} \text{ and} \tag{15}$$

$$\underbrace{\frac{\partial}{\partial t}\widehat{\Delta Alk}}_{\text{tendency}} = \underbrace{-\frac{\partial}{\partial z}\widehat{w\Delta Alk}}_{\text{advection}} + \underbrace{\frac{\partial}{\partial z}\widehat{K\frac{\partial}{\partial z}\Delta Alk}}_{\text{diffusion}} + \underbrace{\frac{\partial}{\partial t}\widehat{\Delta Alk|_{bio}}}_{\text{biology}} + \underbrace{\frac{\partial}{\partial z}\widehat{\Delta f_{Alk}}}_{\text{OAE }\Delta Alk}, \tag{16}$$

where Alk and DIC perturbations between OAE and baseline simulations are represented by ΔAlk and ΔDIC, respectively and the hat symbol over the variable represents the horizontal integral of the corresponding variable over the global ocean. To derive Equations 16 and 15, we assume that ocean circulation and Alk/DIC dilution are not impacted by the OAE deployment, and that for advective and diffusive terms the horizontal components become zero.

Similar to budget equations, Equations 15 and 16 relate $\Delta\widehat{DIC}$ and $\Delta\widehat{Alk}$ tendencies with the advection, diffusion, biology, and OAE additionality (in $\Delta\widehat{DIC}$ equation) or Alk flux (in $\Delta\widehat{Alk}$ equation).

For the 5 continuous Alk experiments, Figures S4 and S5 show the profiles of budget terms for $\Delta\widehat{DIC}$ and $\Delta\widehat{Alk}$. For all of the OAE deployments the response of biological processes was insignificant — the biological source terms were at least 3 orders of magnitude lower compared to the tendency terms for both $\Delta\widehat{DIC}$ and $\Delta\widehat{Alk}$ and are therefore not shown. For clarity, the budget terms are shown only for the last 5 years of simulation; however, they are representative of the entire simulation period.

In addition, the two figures show the mixed layer depth (MLD) as indicative of the interface that separates highly turbulent and relatively well-mixed near-surface layer from the stably-stratified ocean below. The MLD is diagnosed from daily-mean values of ther-

modynamic fields, and since there is considerable uncertainty in characterization of MLD we plot its values from *Boyer* (de Boyer Montégut et al., 2004), *Suga* (Suga & Hanawa, 1990), and *Kara* (Kara et al., 2003) methods.

For the NAS deployment, MLD varies most strongly and is between 400–900-m deep during winter and early spring and shoals to about 50-m during summer. The three MLD depth computations differ, especially during winter and early spring when the MLD is deepest. Boyer and Suga MLD differ the most, with Boyer being consistently shallower, while Kara MLD lies between these two extremes. For NAS, vertical diffusion transports $\Delta\widehat{DIC}$ and $\Delta\widehat{Alk}$ from the surface via a deepening of the MLD, which indicates presence of strong vertical mixing. This transport is strongest when the MLD deepens substantially during winter. Vertical advection transports near-surface $\Delta\widehat{DIC}$ and $\Delta\widehat{Alk}$ into upper-ocean layers (roughly 100-m deep), while it is also responsible for a sink of $\Delta\widehat{DIC}$ and $\Delta\widehat{Alk}$ throughout much of the deeper layer between 200–800 m. This advective transport appears to be fairly independent of MLD dynamics. The tendency of near-surface $\Delta\widehat{Alk}$ exhibits a strong seasonal cycle: $\Delta\widehat{Alk}$ generally increases when the MLD shoals (due to OAE Alk addition). However, when the MLD deepens, even though the Alk is added in the near surface layer, the $\Delta\widehat{Alk}$ decreases at the expense of vertical mixing associated with a deepening of the MLD. Similar dynamics occur for $\Delta\widehat{DIC}$, except that the $\Delta\widehat{DIC}$ budget is impacted by atmospheric CO_2 which also has a strong seasonal cycle peaking in late fall and early winter — just before the MLD begins to deepen.

WBC, ACC, and EBC sites share many similar characteristics, except that for ACC the MLD is out of phase because the deployment is located in the southern hemisphere. MLD dynamics are dominated by strong seasonality and deepen to roughly 200 m during

spring and are shallowest during late summer for the respective hemispheres. For EU, the MLD has weaker seasonality. The three MLD criteria agree well in terms of MLD depth and seasonal variability. As for NAS, the deepening of the MLD is associated with strong vertical diffusion of $\Delta\widehat{DIC}$ and $\Delta\widehat{Alk}$ from the surface within the MLD. Here vertical diffusion tend to overshoot the MLD and indicates either underestimation of MLD by all three MLD criterion or strong vertical mixing that extends beyond the MLD. For both of these locations, advection transports both $\Delta\widehat{Alk}$ and $\Delta\widehat{DIC}$ from near-surface waters to depth. While ACC has weak seasonality in advective transport, it is substantial for WBC. As for NAS, surface-ocean fCO_2 has strong seasonality, which is presumably related to the seasonality of MLD and advective term. This seasonality is less apparent for ACC and EBC. We note that the seasonality of fCO_2 can also be impacted by CO_2 piston velocity.

For EU, due to its location in the tropics, has no discernible seasonal cycle of MLD. Here diffusion generally mixes $\Delta\widehat{Alk}$ and $\Delta\widehat{DIC}$ from the surface downwards and advection, while it exhibit significant temporal variations, generally transports $\Delta\widehat{Alk}$ and $\Delta\widehat{DIC}$ towards the surface. This site also has seasonal transport of $\Delta\widehat{Alk}$ and $\Delta\widehat{DIC}$ below 150-m depth. EU is associated with strong multi-annual variability in pCO_2. For the 5-year shown in Figure S4, the pCO_2 is significantly increased around the start of year 2016.

Text S6. Additional Comparison of rapid-mCDR and ECCO-Darwin model

While the main comparison of rapid-mCDR against ECCO-Darwin is shown in the main text, Figure S6 shows additional comparison of vertically-resolved $mCDR_{equil}$ between rapid-mCDR and ECCO-Darwin, along with its time evolution for all five continuous

experiments and for both both versions of horizontal averaging (rapid-mCDR (Deploy) and rapid-mCDR (HorAdv) see main text, Section 4 for details).

For all five experiments, rapid-mCDR generally captures the ECCO-Darwin profiles of $mCDR_{equil}$. In general, we find that the values with rapid-mCDR (HorAdv) are closer to ECCO-Darwin compared to values from rapid-mCDR (Deploy) which is expected as the former ones accounts for the horizontal advection of OAE perturbation.

References

Carroll, D., Menemenlis, D., Adkins, J. F., Bowman, K. W., Brix, H., Dutkiewicz, S., ... Zhang, H. (2020). The ECCO-Darwin Data-Assimilative Global Ocean Biogeochemistry Model: Estimates of Seasonal to Multidecadal Surface Ocean p CO_2 and Air-Sea CO_2 Flux. *Journal of Advances in Modeling Earth Systems*, *12*(10), 1–28.

Carroll, D., Menemenlis, D., Dutkiewicz, S., Lauderdale, J. M., Adkins, J. F., Bowman, K. W., ... Zhang, H. (2022). Attribution of space-time variability in global-ocean dissolved inorganic carbon. *Global Biogeochemical Cycles*, *36*(3), e2021GB007162.

de Boyer Montégut, C., Madec, G., Fischer, A. S., Lazar, A., & Iudicone, D. (2004). Mixed layer depth over the global ocean: An examination of profile data and a profile-based climatology. *Journal of Geophysical Research: Oceans*, *109*(C12). Retrieved from `https://onlinelibrary.wiley.com/doi/abs/10.1029/2004JC002378` doi: 10.1029/2004JC002378

Gregor, L., & Gruber, N. (2021). Oceansoda-ethz: a global gridded data set of the surface ocean carbonate system for seasonal to decadal studies of ocean acidification. *Earth System Science Data*, *13*(2), 777–808.

Humphreys, M. P., Lewis, E. R., Sharp, J. D., & Pierrot, D. (2022). PyCO2SYS v1.8: marine carbonate system calculations in Python. *Geoscientific Model Development*, *15*(1), 15–43.

Kara, A. B., Rochford, P. A., & Hurlburt, H. E. (2003). Mixed layer depth variability over the global ocean. *Journal of Geophysical Research: Oceans*, *108*(C3). doi: 10.1029/2000JC000736

Olsen, A., Lange, N., Key, R. M., Tanhua, T., Bittig, H. C., Kozyr, A., ... Woosley, R. J. (2020). An updated version of the global interior ocean biogeochemical data product, glodapv2.2020. *Earth System Science Data*, *12*(4), 3653–3678.

Reynolds, R. W., Rayner, N. A., Smith, T. M., Stokes, D. C., & Wang, W. (2002). An Improved In Situ and Satellite SST Analysis for Climate. *Journal of Climate*, *15*(13), 1609–1625.

Suga, T., & Hanawa, K. (1990). The mixed-layer climatology in the northwestern part of the North Pacific subtropical gyre and the formation area of Subtropical Mode Water. *J Mar Res*, *48*(3), 543–566. doi: 10.1357/002224090784984669

Wang, H., Pilcher, D. J., Kearney, K. A., Cross, J. N., Shugart, O. M., Eisaman, M. D., & Carter, B. R. (2023). Simulated impact of ocean alkalinity enhancement on atmospheric CO_2 removal in the bering sea. *Earth's Future*, *11*(1), e2022EF002816.

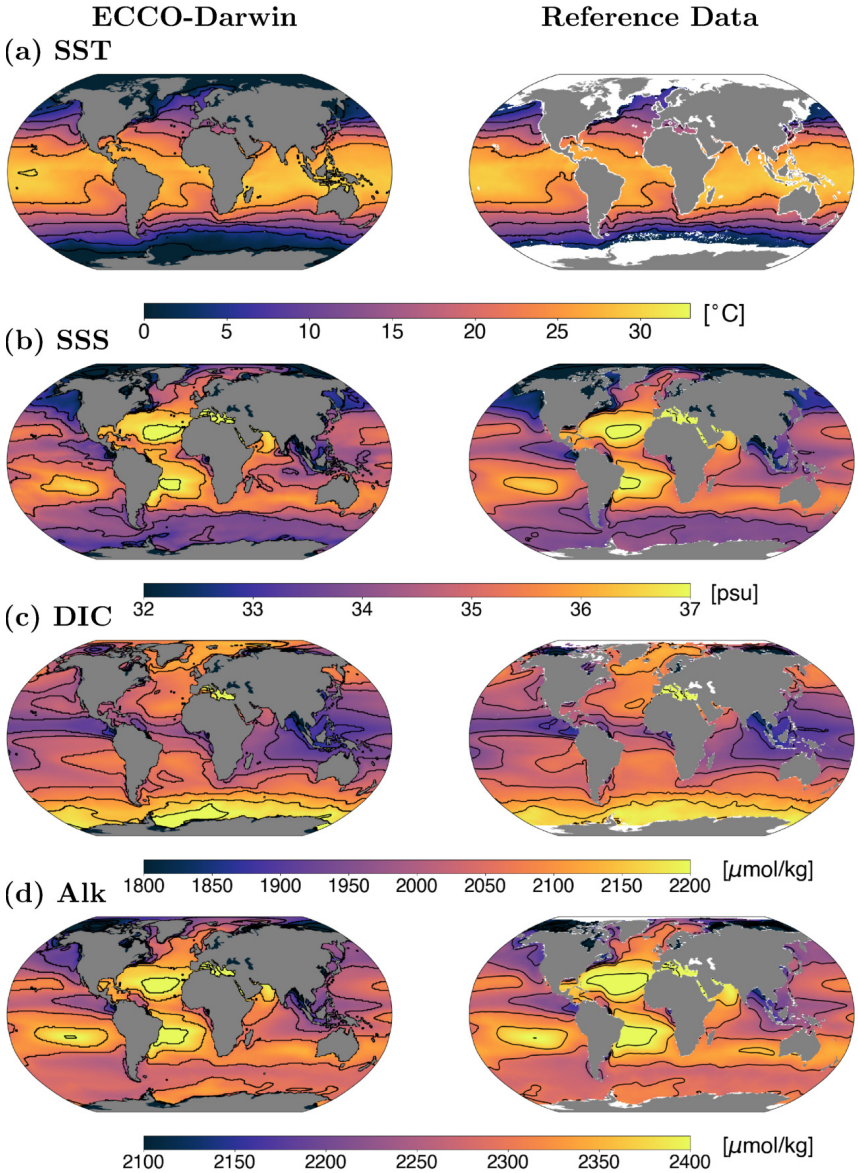

Figure S1. Comparison of time-mean (from January 1995 to December 2017) surface-ocean fields from the baseline ECCO-Darwin simulation against reference (a) sea-surface temperature (SST), (b) sea-surface salinity (SSS), (c) DIC, and (d) Alk. Reference SST is from Reynolds et al. (2002); all other reference fields are from OceanSODA-ETHZ (Gregor & Gruber, 2021).

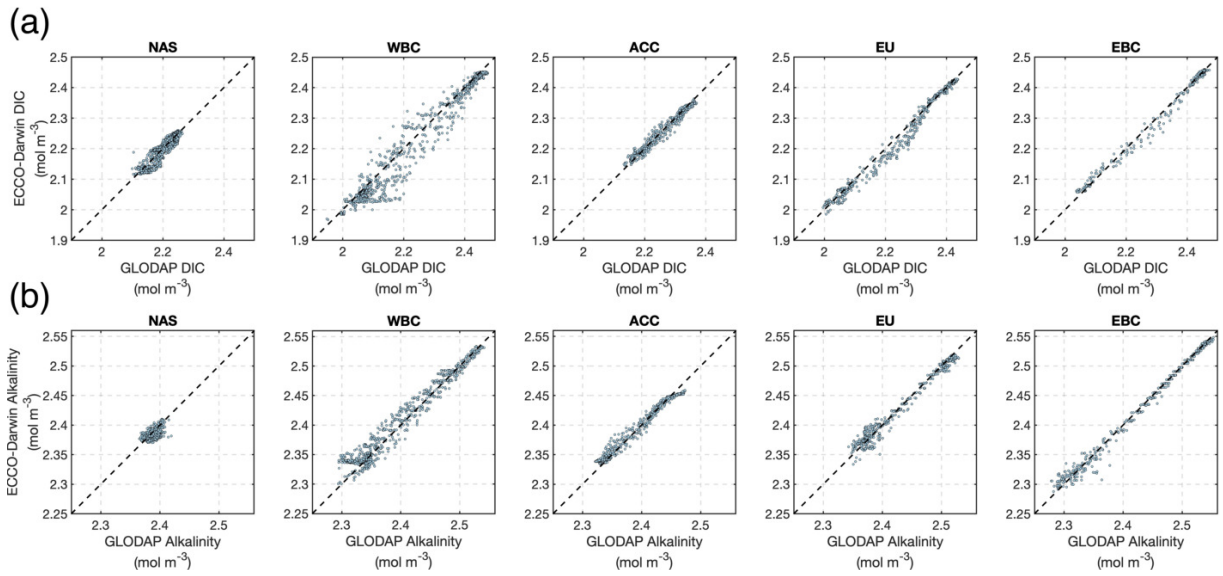

Figure S2. Comparison of the baseline ECCO-Darwin DIC and Alk against all GLODAPv2.2022 observations at the 5 deployment sites. The x-axis shows observations and y-axis shows the corresponding monthly-mean model value taken at the closest space-time location.

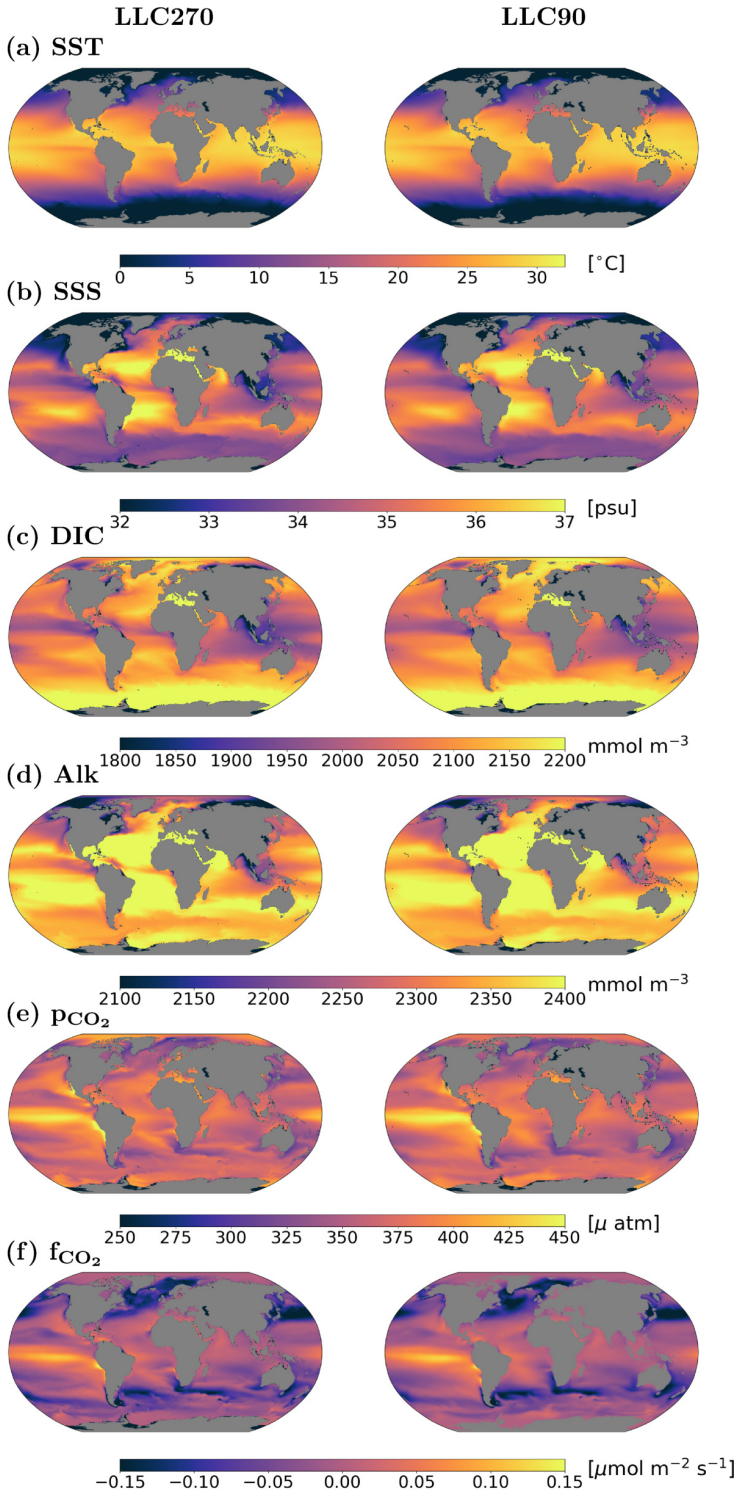

Figure S3. Comparison of time-mean (1995–2017) surface-ocean fields from ECCO-Darwin LLC 270 (Carroll et al., 2020) and the baseline ECCO-Darwin (LLC90 solution) used in this paper.

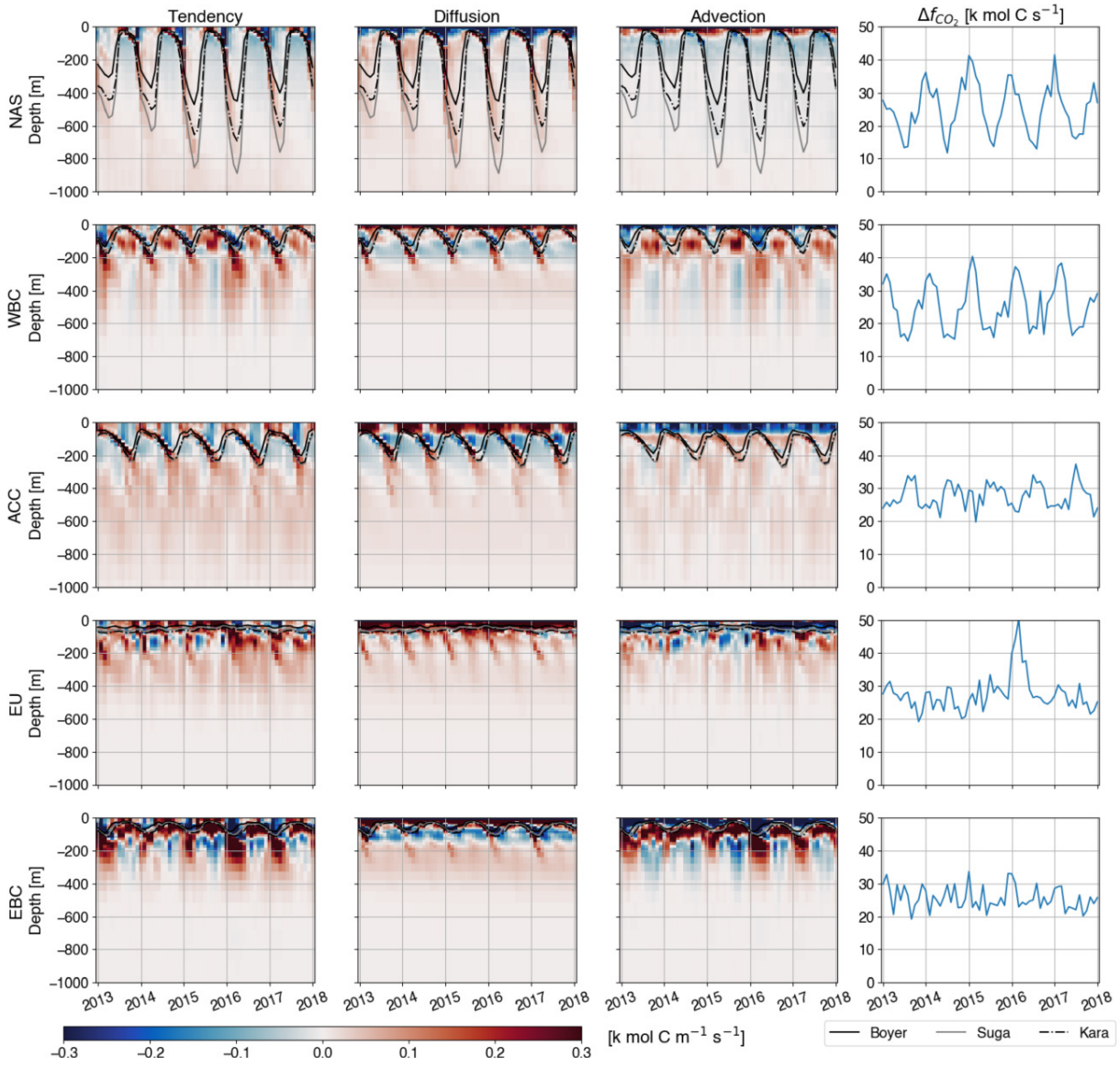

Figure S4. Horizontally-integrated budget terms from $\Delta\widehat{DIC}$ (Equation 15) for the 5 continuous OAE experiments over the last 5 years of simulation. Budget terms include: tendency, diffusion, advection, and air-sea CO_2 flux. Biological source terms are negligible and not shown. Three different mixed layer depth (black lines) are computed using Boyer, Suga, and Kara diagnostics and we plot the spatial-mean values over the OAE deployment sites.

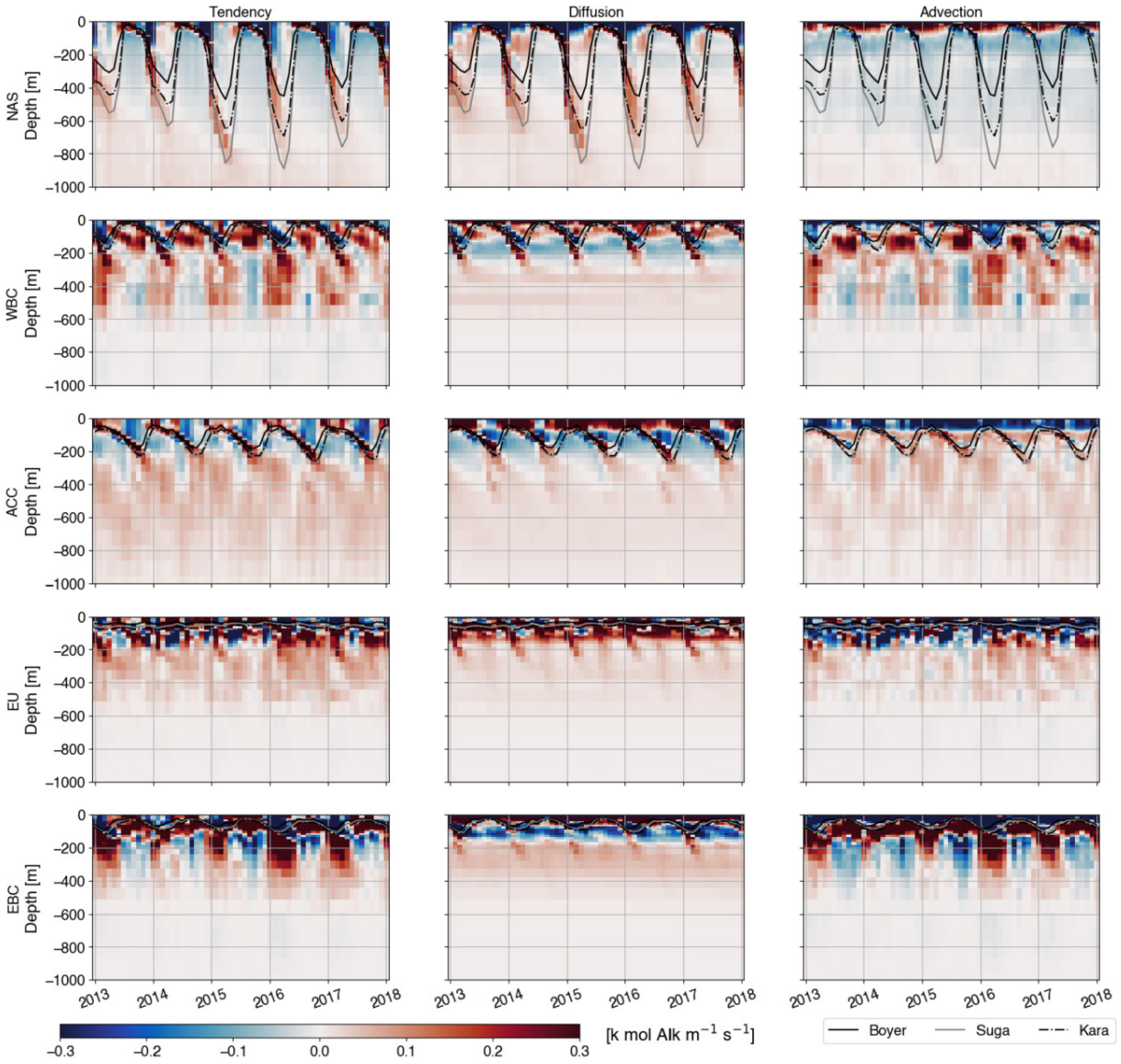

Figure S5. Horizontally-integrated budget terms for $\Delta\widehat{Alk}$ (Equation 16) for the 5 continuous OAE experiments over the last 5 years of simulation. Budget terms include: tendency, diffusion, and advection. Biological source terms are not shown because they are negligible; prescribed surface-ocean Alk flux is constant and is also not shown. Three different mixed layer depth (black lines) are computed using Boyer, Suga, and Kara diagnostics and we plot the spatial-mean values over the OAE deployment sites.

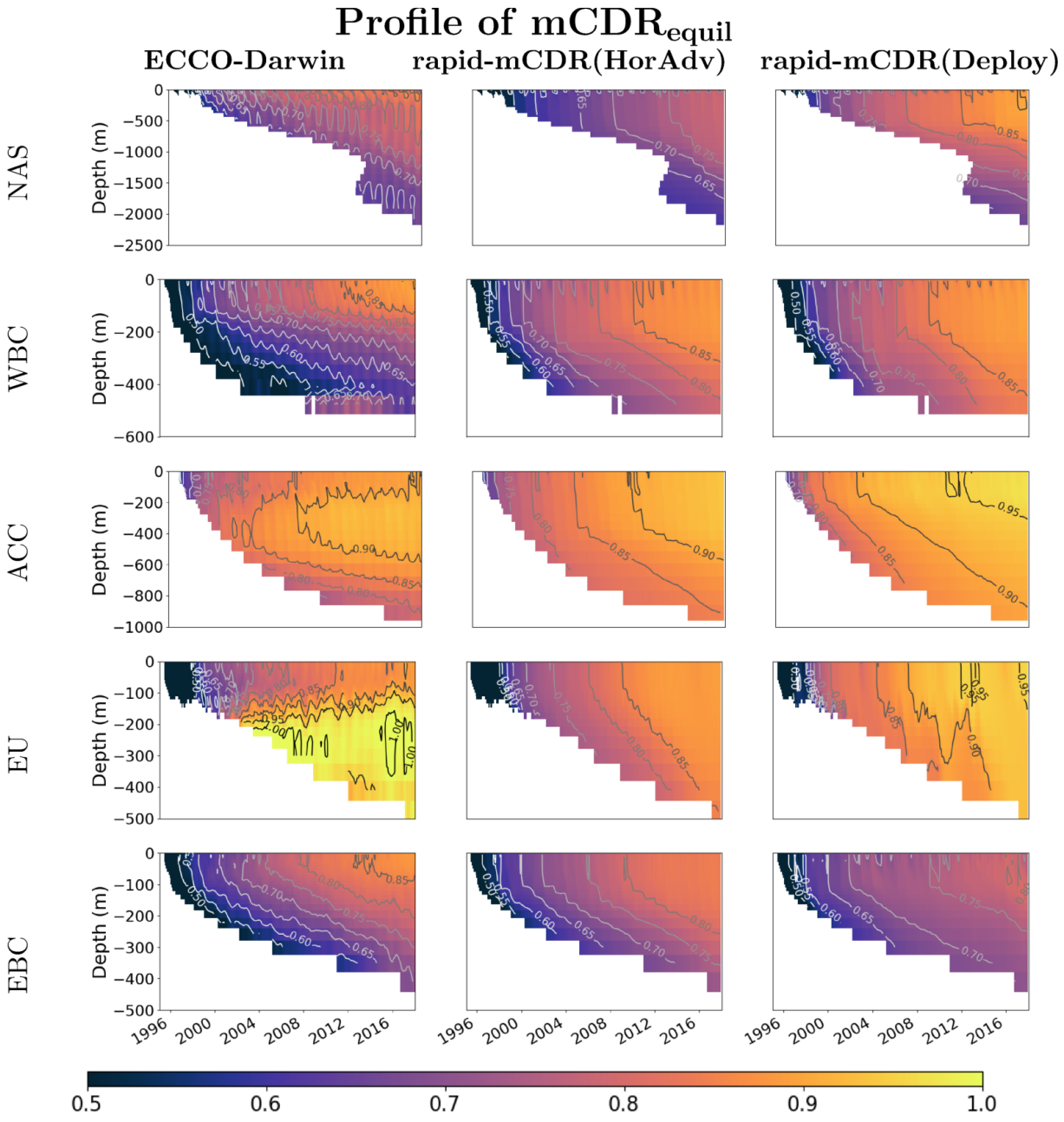

Figure S6. Comparison of time series of horizontal-mean, vertically-resolved $mCDR_{equil}$ from ECCO-Darwin (left panel) and both versions of rapid-mCDR (middle and right panels).